Chemical Geology 649 (2024) 121966

Contents lists available at ScienceDirect

Chemical Geology

journal homepage: www.elsevier.com/locate/chemgeo

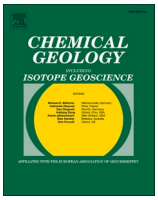

Effects of phosphate on REY adsorption by goethite: Insights into REY enrichment and release in marine iron oxyhydroxides during early diagenesis

Yongjia Liang [a], Xiaoming Sun [a,b,*], Dengfeng Li [b,*], Caroline L. Peacock [c], Yu Fu [b]

[a] School of Earth Sciences and Engineering, Guangdong Provincial Key Laboratory of Geodynamics and Geohazards, Sun Yat-sen University, Zhuhai 519802, China.
[b] School of Marine Sciences, Guangdong Provincial Key Laboratory of Marine Resources and Coastal Engineering, Zhuhai 519082, China
[c] School of Earth and Environment, University of Leeds, Leeds LS2 9JT, UK

ARTICLE INFO

Editor: Hailiang Dong

Keywords:
Goethite
Rare earth elements
Phosphate
Recrystallization
XAFS

ABSTRACT

Deep-sea REY (lanthanides and yttrium) can be initially scavenged by nano ferromanganese (oxyhydr)oxides via ion adsorption and lattice substitution, while subsequent aging and partial recrystallization induced by reduction during diagenesis usually cause release and redistribution of REY. Previous studies find positive correlations among REY, goethite (α-FeOOH) and phosphorus/phosphate in some marine (micro)nodules, but the mechanism responsible for these correlations is yet unclear. The interaction between iron oxyhydroxides and metal oxyanions has been studied extensively, but no study focuses on interactions between iron oxyhydroxides, REY, and phosphate. This study investigates the immobilization and release mechanisms of REY by synthetic goethite at macro- and molecular scales by comprehensive usage of ad/desorption experiments, inductively coupled plasma mass spectrometry, X-ray absorption fine structure (XAFS) spectroscopy, and density functional theory calculations. The results indicate that goethite exhibits an adsorption preference for heavy REY, displaying obvious lanthanide tetrad effects. Phosphate (0.02 mM $\leq C_P \leq$ 0.2 mM) however, greatly enhances REY adsorption by forming ternary complexes, particularly light REY. EXAFS interpretations further confirm the formation of ternary complexes in La-adsorbed samples, and that phosphate can link trivalent REY and goethite on the surface. Moreover, some Ce^{III} is further oxidized to Ce^{IV} with the help of dissolved oxygen. These observations illuminate how phosphate contributes to rare earth enrichment during early diagenesis. As goethite recrystallization is common in hypoxic environment, we further monitored REY behavior during recrystallization and find that previously adsorbed La/Ce and phosphate are released and combined to form $LaPO_4$/$CePO_4$ precipitates. Importantly, the Ce^{IV} reduced during recrystallization indicates that the positive Ce anomaly is likely to pass down, potentially explaining why a positive Ce anomaly is observed in diagenetic nodules and apatite at lower depth. Our study provides insights into the role of phosphate in REY-adsorption on goethite and possible mechanisms of REY enrichment, and desorption during early diagenesis, corresponding with REY patterns observed in marine iron oxyhydroxides.

1. Introduction

REY (lanthanides and yttrium) are a group of 16 elements sharing similar chemical and physical properties. They are economically important and widely used in a variety of industrial applications, including electronics, clean energy, aerospace, and automotive industries. REY can be found in the Earth's crust (Weng et al., 2015) and shallow deep-sea sediments (Pattan et al., 1995; Kato et al., 2011). Global deep-sea samples of the Pacific, Indian, Atlantic and Arctic Ocean suggest that deep-sea sediments are a potential REY reservoir with high ΣREY concentrations (up to ~8000 ppm within 10 msbf; meters below seafloor; Yasukawa et al., 2018) (Fig. 1 and Table S1). To facilitate future use of deep-sea REY, research on REY enrichment in and extraction from deep-sea deposits is booming.

Ferromanganese (micro)nodules are the major hosts of deep-sea REY next to bioapatite (mostly fish debris) and may help transfer REY to bioapatite (Takahashi et al., 2015). REY contents of (micro)nodules in REY-rich muds, generally being diagenetic or hydrogenetic, can reach

* Corresponding authors.
E-mail addresses: eessxm@mail.sysu.edu.cn (X. Sun), lidf3@mail.sysu.edu.cn (D. Li).

https://doi.org/10.1016/j.chemgeo.2024.121966
Received 18 November 2023; Received in revised form 25 January 2024; Accepted 28 January 2024
Available online 1 February 2024

up to 1000–3500 ppm (Dekov et al., 2003; Li et al., 2020a). The major mineral phases of ferromanganese (micro)nodules are ferromanganese (oxy)hydroxides/oxides (e.g., Mn phase mineral: δ-MnO_2, vernadite, birnessite, todorokite; Fe phase mineral: FeOOH, ferrihydrite, and goethite; Vereshchagin et al., 2019). The laser ablation (LA) ICP-MS spots and laser element mappings of these (micro)nodules show that REY (except for cerium) are positively correlated with Fe and P-bearing components (Zhou et al., 2020; Li et al., 2020b; Fig. 2 and Table S2), which are subsequently identified as goethite by X-ray diffraction (XRD) and transmission electron microscopy (TEM; Zhou et al., 2020; Li et al., 2020b). While near the East Pacific Rise, some REY-rich sediments show similar positive correlations with both Fe and P, suggesting the important role of iron oxyhydroxides and P in the formation of REY-rich (micro)nodules and muds (Kashiwabara et al., 2018).

Iron oxyhydroxides, including ferrihydrite and goethite, serve as crucial environmental sorbents of metals in the soil settings (Cornell and Schwertmann, 2003). These Fe-bearing minerals in (micro)nodules also affect the geochemical cycling of metals in the marine environment, particularly critical metals including REY (Takahashi et al., 2007). A wealth of previous research shows that iron oxyhydroxides adsorb metal cations via outer-sphere complexation (physical interaction), inner-sphere complexation, and/or isomorphic substitution (e.g., Cornell and Schwertmann, 2003; Liu et al., 2021). The first work concerning the surface adsorption of seawater REY on goethite reports that α-FeOOH non-selectively adsorbs REY from seawater, while crystalline goethite preferentially scavenges light REY (La—Eu) (Koeppenkastrop and De Carlo, 1992). On the contrary however, two later studies show that iron oxyhydroxide tends to adsorb more heavy REY (Gd—Lu, Y) at pH > 6.2, with REY showing an apparent M-type lanthanide tetrad effect (Bau, 1999; Ohta and Kawabe, 2001), and meanwhile Ce oxidation weakens as adsorption progresses (Bau, 1999). These studies investigate the REY patterns on goethite at conditions pertinent to seawater and hot spring environments. However, the adsorption mechanisms and the effects of anions on REY adsorption, which are ubiquitous in seawater and porewater, are unknown. According to previous studies, phosphate can couple with goethite and enhance the adsorption of some metal cations on goethite (Antelo et al., 2005; Hinkle and Catalano, 2015; Liu et al., 2021), yet how and why goethite is positively correlated with P in REY-rich (micro)nodules is unclear. Furthermore, during early diagenesis, (micro)nodules often undergo reduction and oxyhydroxides such as goethite are generally recrystallized and dissolved in the presence of Fe^{II} under hypoxic conditions (Gorski and Fantle, 2017). Besides numerous cations and oxyanions can be reduced by adsorbed-Fe^{II} on synthetic goethite or hematite as reported, such as U^{VI}, Tc^{VII}, and arsenate (Antelo et al., 2005; Jaisi et al., 2009; Taylor et al., 2017). Previous X-ray absorption fine structure (XAFS) spectroscopy analyses suggest that some elements (e.g. Ni and Sc) can incorporate into the goethite lattice during recrystallization (Hinkle and Catalano, 2015; Qin et al., 2021). Nevertheless, nothing is known about the effects of this process on REY redistribution in (micro)nodules during diagenesis. REY have large ionic radius (ionic radius of light REY in 9-fold coordination and heavy REY in 8-fold coordination: 1.216–0.977 Å; Shannon, 1976; Borst et al., 2020) and are unlikely to substitute into the goethite lattice (Cornell and Schwertmann, 2003).

Here we discuss the effects of inorganic P (phosphate) on REY adsorption by goethite, therefore we pay attention to the adsorption mechanisms of REY on goethite with and without phosphate. Then we investigate the behaviors of REY during the recrystallization of goethite in the presence of phosphate in Fe^{II}-containing hypoxic conditions. At the molecular level, we use XAFS analyses combining with density functional theory (DFT) calculations and X-ray adsorption near edge structure (XANES) to investigate the adsorption configurations of REY on goethite and monitor the valence of Ce after adsorption and recrystallization in the presence of phosphate, respectively. At last, we try to present an improved understanding of REY enrichment in marine ferromanganese (micro)nodules during early diagenesis focusing on La and Ce based on the results.

2. Materials and methods

2.1. Materials

Chemical reagents, including $NaH_2PO_4{\cdot}H_2O$ (> 98%) and $FeCl_4{\cdot}4H_2O$ (> 99.95%) from Shanghai Macklin Biochemical Co., Ltd., $Fe(NO_3)_3{\cdot}9H_2O$ (>98%) from Alfa Aeser and goethite from Sigma-Aldrich were both used as received. HNO_3, NaOH, and HCl of analytical grade, obtained from Guangzhou Chemical Reagent Factory, were further distilled with DST-1000 Acid Purification Systems. The characteristics of different samples were determined by XRD (Fig. S1) and high-resolution transmission electron microscopy (HRTEM; Fig. S2), and the detailed information of XRD and HRTEM is in section 2.5.

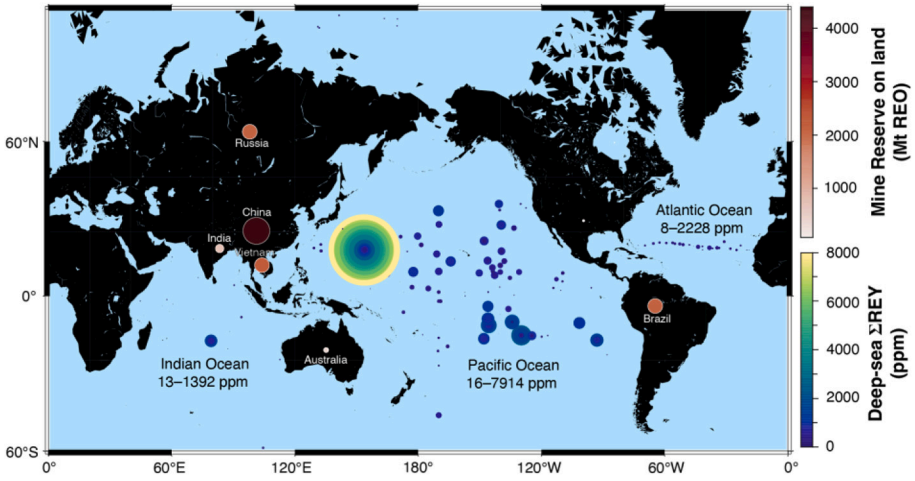

Fig. 1. Estimated marine rare earth and World Mine Reserves. Data of world mine reserves is from USGS (2022). Contents of ΣREY at different surface layers within 10 m samples of deep-sea sediments from the Pacific, Indian, Atlantic and Arctic oceans (Kato et al., 2011; Yasukawa et al., 2016; Menendez et al., 2017; Mimura et al., 2019; Zhang et al., 2019; Tanaka et al., 2020; Sattarova et al., 2023). The cores are collected during KR13, MR13, MR14, MR15 KR13, KR14 and the 30th DaYang cruises, DSDP and ODP expeditions; the piston core samples are obtained from the Ocean Research Institute of the University of Tokyo; box corer are from cruises 77 and 83 of the R/V "Akademik Lavrentyev". For detailed data of deep-see sediments see Table S1. The map was created by using the Python interface for the Generic Mapping Tools (PyGMT) v0.7.0.

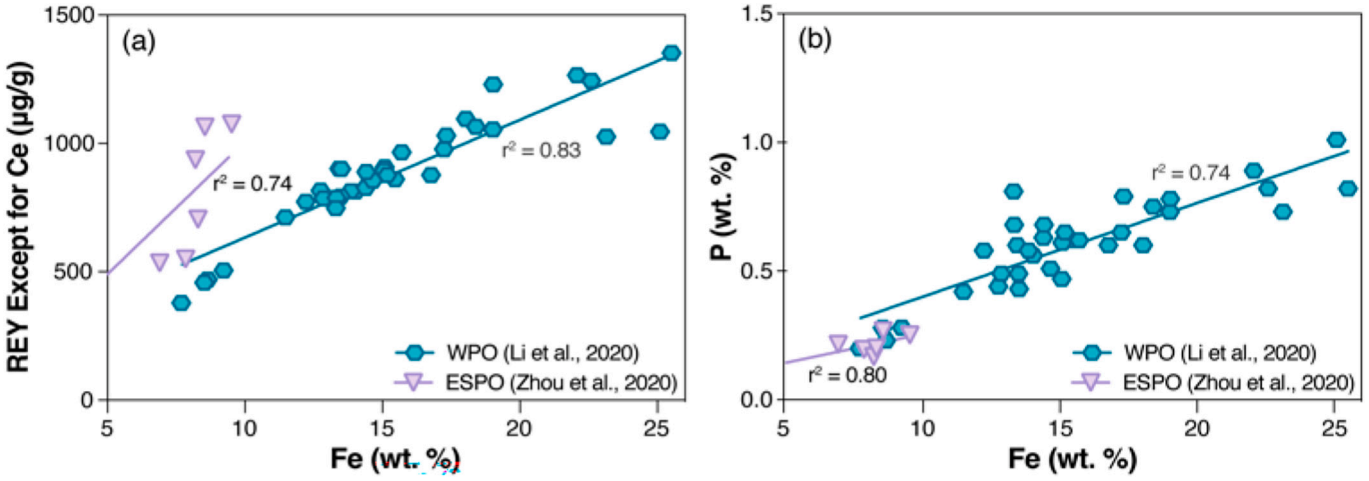

Fig. 2. Correlation of Fe content with REY (exclusion of Ce) (a) and P content (b). a, correlation between Fe and REY (exclusion of Ce) contents in different marine nodule samples of ESPO (Eastern South Pacific Ocean; Zhou et al., 2020) and WPO (Western Pacific Ocean; Li et al., 2020b); b, correlation between Fe and P contents in different marine nodule samples. For detailed data see Table S2.

2.2. Batch adsorption experiments

Background solution of $NaNO_3$ was prepared by mixing NaOH and HNO_3. The stock solution of REY was prepared by using background solution to dilute the multi-elements standard solution of REY and Sc (GNM-M160181-2013B; 100 mg/L of each REY in 5% HNO_3), from Guobiao (Beijing) Testing & Certification Co., Ltd. (GBTC). Another stock solution of La, Ce and Lu was diluted to 10 mg/L with each standard solution (100 mg/L in 5 HNO_3, from GBTC) with same background solution. Herein, La and Lu were selected to represent light and heavy REY, respectively. Meanwhile, as a redox-sensitive element, Ce was also investigated. The Fe^{II} solution was prepared as described by Qin et al. (2021) in an anaerobic chamber (Ar: 98%; H_2: 2%) with an oxygen concentration of <0.8 ppm. The pH of all stock solutions was adjusted by adding a small amount (<20 μL) of 0.05 M NaOH and 0.05 M HNO_3.

Before batch adsorption, the kinetics of REY adsorption was first studied by adding 100 mg goethite to a 0.1 mg/L REY solution (0.01 M HNO_3). Then we investigated the adsorption of REY on goethite and how phosphate, pH, ionic strength (IS) and carbonate affect this process. According to previous research: 1) REY concentrations in ferromanganese (micro)nodules generally range from 100 to 3500 ppm; 2) Phosphate contents of porewater can reach up to 0.02 mM in shallow deep-sea sediments (Dekov et al., 2003; Mizell and Hein, 2015); 3) REY ions in seawater generally complex with carbonate and form REY-carbonate ions (Tang and Johannesson, 2010). Therefore, different REY/REY-carbonate ($C_{REY} = C_{REY\text{-}carbonate}$ = 0.1, 0.2, 0.5 or 1 mg/L; 20 mL) and phosphate stock solutions (C_p = 0.02, 0.04, 0.2 mM; 20 mL) were prepared. In group goethite, goethite (100 mg) and different REY/REY-carbonate stock solutions were added to 50 mL centrifuge tubes (polypropylene). Here, sample G-0.1 means sample with initial C_{REY} = 0.1 mg/L, while samples GC-0.1 represents sample treated with 0.1 mg/L REY-carbonate, and so does others. In group goethite + phosphate, the same amount of goethite was first reacted with different phosphate stock solutions. After 24 h, the mixture was centrifuged at 4000 rpm for 10 min, and phosphate-adsorbed goethite was separated from the previous solution and rinsed with 1 mL MQ for three times. Then, the phosphate-adsorbed goethite reacted with different REY/REY-carbonate stock solutions (0.1, 0.2, 0.5 or 1 mg/L; 20 mL). Similarly, sample GP0.02–0.1/GPC0.02–0.1 is tread with 0.02 mM phosphate and 0.1 mg/L REY/REY-carbonate sequentially. IS of both reaction groups was set to 0.01 M HNO_3. Each sample was thoroughly mixed by a vortex mixer and then placed in an oscillator at room temperature. The pH of REY-carbonate adsorption on goethite was set to 7.8. However, the REY adsorption experiments were carried out under pH 6.8 to avoid precipitation (Table S3). REY-adsorption on goethite at different pH (2−12) and IS (0.01 and 0.5 M $NaNO_3$) was also performed, and the other reaction conditions were the same as before.

After adsorption, all the samples were centrifuged at 4000 rpm for 10 min and the supernatant was filtered by a MillexGP 0.22 μm filter-unit. The filtrate was subsequently diluted with 2 vol% purified nitric acid and analyzed with Agilent 7700 ICP-MS (inductively coupled plasma mass spectrometry) equipped with an Agilent ASX-500 auto-sampler. A multi- element standard solution (GNM-M160181-2013B) was used to prepare the external standards of 0, 0.1, 0.5, 1, 2, 5, 10, 20, 50, 100 μg/L in 2% HNO_3. The Residues of samples were digested with 10 M HCl in centrifuge tubes after 24 h and then evaporated at 80 °C. After dissolved in 1 mL HNO_3, they were diluted to 50 mL for ICP-MS analysis to calculate their recoveries. And the recoveries (91.2–108.5%) showed that the experiments are reliable.

According to the detection limits of TEM, HRTEM and XAFS, an additional adsorption experiment was conducted to obtain better analytical results of La, Ce and Lu. The phosphate-adsorbed goethite (samples GP0.2–5 and GP0.2–10) was added to 20 mL La + Ce + Lu solutions ($C_{La} = C_{Ce} = C_{Lu}$ = 5 mg/L or 10 mg/L). After the adsorption experiment, the solid phase was also separated and rinsed with Milli-Q water. Residues were dried in a freeze-drying machine and packed into polyethylene bags.

2.3. Desorption

10.0 mmol/L of CH_3COONH_4 solution and 2.0 mmol/L of EDTA-2Na solution were added to sequentially extract adsorbates on goethite. In general, CH_3COONH_4 leaches ions fixed on goethite via ion exchange, and EDTA-2Na extracts the chelated species. As for the residues, they can be the products of more stable inner complexes or surface precipitation (Borst et al., 2020; Qin et al., 2021).

2.4. Recrystallization experiments

Goethite recrystallization was conducted on samples GP0.2–5 and GP0.2–10 after batch adsorption. Firstly, the supernatant was separated from the residue after centrifugation at 4000 rpm for 10 min, purged with pure nitrogen for 45 min, and then stirred for 24 h exposing in an anaerobic chamber to remove residual dissolved oxygen. After that, each of the deoxygenated supernatant along with 1 mM Fe^{II} solution was mixed with corresponding solid. After reacting and aging in anaerobic chamber for 21 days, the solid products were rinsed thoroughly, and then naturally dried before packed into polyethylene bags.

To identify the occurrence of lattice substitution during recrystallization, La-/Lu-substituted goethite was synthesized after Persson et al. (1996) and Qin et al. (2021). Take La-substituted goethite for example, a 90 mL of 5.0 mol/L KOH solution was added to a bottle containing 50 mL of 1.0 mol/L (Fe + La)$(NO_3)_3$ solution, and the molar ratios of Fe and La in different substitution samples are 9:1, 49:1 and 99:1. Then the suspension was aged at 70 °C and mildly shaken on an orbital oscillator at 20 rpm. After 14 days, solid phase was separated and washed in a 3.0 mol/L H_2SO_4 solution at 45 °C for 2 h. Finally, wash the solid with Milli-Q water until the solution pH reaches to ~7.0 to remove possible adsorbed species and precursors of goethite.

2.5. Structures and morphology of samples using XRD, SEM and TEM analyses

XRD analyses were finished on Rigaku Rapid II X-ray diffraction in the School of Marine Sciences, Sun Yat-sen University, operated at 50 kV and 30 mA with Mo *Kα* radiation and at a scan rate of 1°/min with a 0.02° step.

SEM observation was done by TESCAN MIRA at an accelerating voltage of 20 kV in the School of Marine Sciences, Sun Yat-sen University. HRTEM data was obtained by the FEI Talos F200S TEM at Guangzhou Institute of Geochemistry, Chinese Academy of Sciences (GIGCAS), operating at 200 kV. For preparation, a few of the samples were sonicated in the ultra-pure acetone for 30 min. Suspensions were pipetted onto an ultrathin lacy-carbon-coated HRTEM Cu-grid and then dried at room temperature. These samples were analyzed for goethite morphology and elemental distribution. HRTEM was equipped with a bright field (BF) detector, a high angle annular dark field (HAADF) detector, and an energy dispersive X-ray spectroscopy (EDS). EDS mapping was applied to characterize the Fe, P and REY distributions, and corresponding semi-quantitative results were obtained with detection limit of 0.1%.

2.6. Adsorption mechanisms inferred by XAFS analyses and DFT calculation

To better understand how REY are adsorbed in the presence of phosphate, La was selected to study the behavior of non-redox sensitive rare earth elements on goethite before and after recrystallization in the presence of phosphate, and meanwhile, the valance of redox sensitive Ce was observed. To avoid interference between two elements, La-L_1 XAFS and Ce-L_3 XANES of samples were analyzed. XANES and XAFS data were obtained by BL14W1 at Shanghai Synchrotron Radiation Facility. Quantum chemical calculations were performed in Quantum Espresso to obtain the geometry of the surface complex model of goethite (Giannozzi et al., 2009). The Kohn-Sham equation-based Quantum Espresso code was employed to implement the DFT calculation. To define the exchange-correlation energy, the generalized gradient approximation of Perdew-Burke-Ernzerhof (GGA-PBE) was selected (Sancho-García et al., 2003). G-centered 4 × 4 × 4 Monkhorst-Pack grid was chosen to sample the Brillion zone of the systems. For self-consistent calculation, the energy and charge density criteria were set to 1×10^{-6} eV for convergence. Note that the experimental lattice constant and atomic coordinates were used for the calculation and the spin-orbit interaction (SOI) was not considered for the band structure calculation. For energy calculations, the formation energy was calculated following formula: E(total) = E (top) – 2E(base), where E(total), E(top) and E(base) are the energy of the total system, surface adsorbate and -FeOH base, respectively.

3. Results

3.1. Adsorption kinetics

Kinetics data for REY adsorption on goethite at C_{REY} = 0.1 mg/L demonstrates a rapid adsorption rate of REY (~ 45%) within 2 h, and equilibrium is attained after 8 h (Fig. 3a and Table S4). To obtain equilibrium in the following batch experiments, the reaction time is set to 24 h. Two fitting models, pseudo-first-order and pseudo-second-order models are applied to simulate the adsorption kinetics data (Wu et al., 2018; Qin et al., 2021). As shown in Fig. 3a, the kinetic data agrees better with the pseudo-second-order model (R^2 = 0.98) instead of the pseudo-first-order model (R^2 = 0.83). According to the simulation results, REY adsorption on goethite is mainly controlled by chemical adsorption rather than mass transport or physical interactions (Wu et al., 2018).

3.2. Adsorption behavior

3.2.1. Effects of pH, ionic strength

According to Fig. 3b and Table S5, REY adsorption on goethite is pH-dependent both in group goethite and goethite + phosphate, suggesting that the adsorption capacity of goethite for REY varies with pH, similar to that of other metal cations (Peacock and Sherman, 2004; Antelo et al., 2005). Overall, the percentage adsorption of group goethite increases with pH, from ~13% at pH 4.0 to ~65% at pH 8.1. This can be explained by the REY species and the surface properties of goethite. As calculated by Visual MINTEQ ver. 3.1 (Gustafsson, 2018), the REY species are all positively charged at pH 2 to 12. Notably, at pH > 6.8, the precipitation of REY not complexed by carbonate inevitably contributes to the high percentage adsorption, especially at high pH (e.g., pH = 9.8) (Fig. 3b and Table S5). With the presence of phosphate during adsorption, however, the adsorption percentage reaches ~100% at even low pH, 5.7 for C_p = 0.02 mM and 3.0 for C_p = 5 mM (Fig. 3b and Table S5).

Apart from low pH, high ionic strength (IS) can also decrease the REY adsorption. In adsorption groups with different IS, 0.01 and 0.5 M $NaNO_3$, average REY adsorption in high IS samples reduces by nearly 64%, from 82.33% to 18.27% in samples GP0.2–1, and 10.59% to 2.95% in samples G0.1 (Fig. S3; Table S6).

3.2.2. Effects of phosphate on REY/REY-carbonate adsorption

Compared to group goethite, REY adsorption in group goethite + phosphate is much higher in different REY solutions (Figs. 3c-f and Table S7). The adsorbed phosphate on goethite improves the REY adsorption to ~100% (Figs. 3c–f), especially in solutions with high REY concentrations (Figs. 3e–f). As a result, the adsorption capacities of REY on goethite with phosphates range from ~2000–3000 ppm. More importantly, the REY patterns in different adsorption groups also differ. In group goethite, goethite preferentially adsorbs heavy REY, showing an obvious lanthanide tetrad effect, which becomes stronger as REY concentrations of the solution increase (Figs. 3c–f). The lanthanide tetrad effect, also called M type lanthanide tetrad effect, demonstrates the REY partition patterns comprised of four upward-curved segments (La—Nd, Nd—Gd, Gd—Ho and Ho—Lu), showing the shape of two "M" (Masuda and Ikeuchi, 1979). However, with phosphate the adsorption of light REY greatly increases from <50% to 100% as phosphate concentration rises to 0.2 mM (Fig. 3f). As a result, the fractionation between light and heavy REY decreases and the tetrad effect becomes weaker (Figs. 3e–f).

Adsorption of REY-carbonate on goethite are presented in Fig. S4 (see the data in table S8), with errors better than 2%. According to the results, almost all the REY-carbonate complexes (~ 90%–100%) are scavenged by both group goethite and group goethite + phosphate even with high initial REY-carbonate concentration (1 mg/L). In samples with high $C_{REY\text{-}carbonate}$ (Figs. S4c-d), the adsorption rates of heavy REY are ~10% lower than that of light REY, which is opposite to the results demonstrated by samples without carbonate.

3.3. Desorption experiments

During the desorption experiments, a relatively small proportion of REY (<10%), especially heavy REY (Table S9), is extracted by

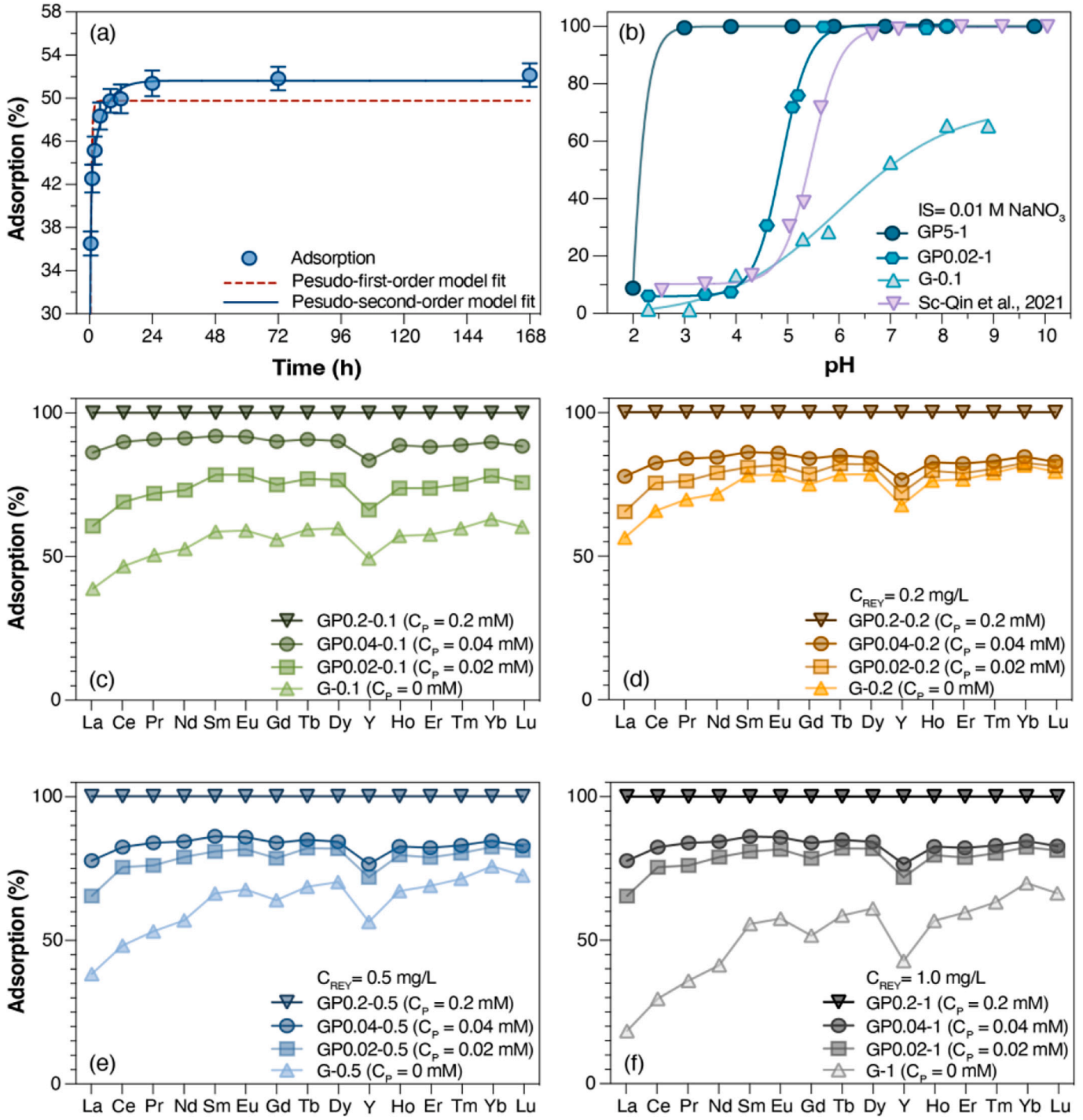

Fig. 3. Adsorption of REY by time (a), pH (b) and of different initial REY concentrations (c-f) in group goethite and goethite + phosphate. a, kinetic data and corresponding model fits for REY adsorption on goethite (T = 293 K, pH = 6.8, M_{Gth} = 0.1 g/L, C_{REY} = 0.1 mg/L, IS = 0.01 mol/L $NaNO_3$ b, effects of pH on the adsorption of C_{REY} with or without phosphate (T = 293 K, M_{Gth} = 0.1 g/L, C_{REY} = 1 mg/L, C_{Sc} = 10 mg/L, IS = 0.01 mol/L $NaNO_3$, 24 h), and the Sc data is obtained from Qin et al. (2021); c-f, batch adsorption of group goethite and goethite + phosphate under different C_{REY} and C_P (T = 293 K, pH = 6.8, M_{Gth} = 0.1 g/L, IS = 0.01 M $NaNO_3$, 24 h).

CH_3COONH_4, while ~12–70% of REY is leached by EDTA-2Na solution. The results show that less heavy REY are leached by either extraction eluents (Table S9), and EDTA-2Na solution can leach more REY than CH_3COONH_4 solution, especially in samples with phosphate. Besides, compared to the samples with no phosphate, the total desorption rates of REY extracted by two complexing agents has significantly increased except for samples with high REY concentrations (C_{REY} = 1 mg/L), from ~32% to the maximum of ~95%.

3.4. Mineralogy and REY behavior before and after goethite recrystallization

The XRD patterns of samples with and without phosphate are identical to the standard pattern of goethite (Fig. S5), indicating no new substance formed after REY adsorption. Similarly, no substance other than goethite is found in SEM image (Fig. 4a). After 21 days of recrystallization in Fe^{II} solutions however, the surfaces of REY-adsorbed

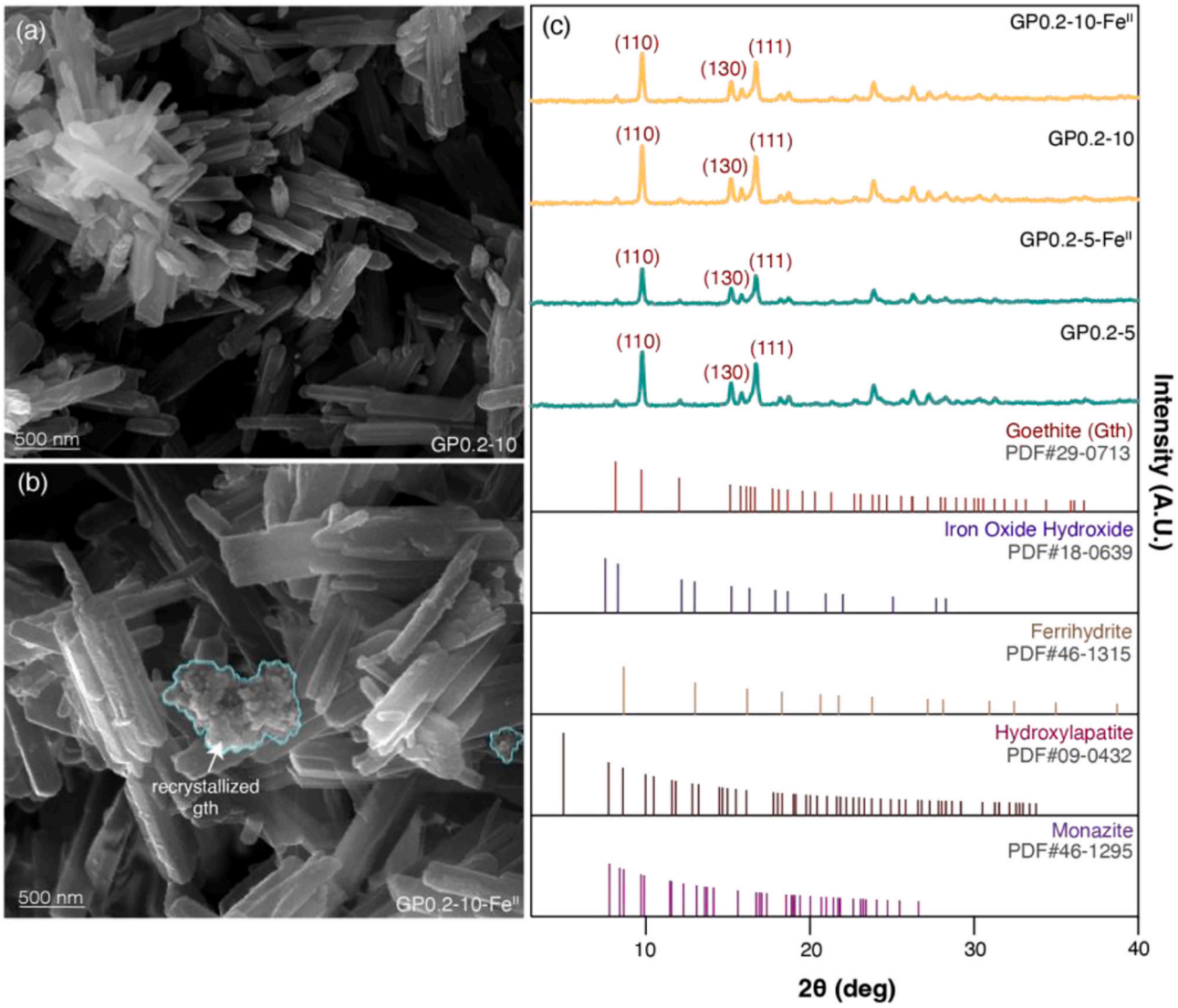

Fig. 4. XRD, SEM results of the REY-adsorbed samples. a-b, SEM images of GP0.2–10 and GP0.2–10-Fe^{II} with an accelerating voltage of 30 kV; c, XRD patterns of REY-adsorbed samples before and after recrystallization (radiation of Cu *K*α).

goethite become rough, and clusters of nano-phase substances are observed (Fig. 4b). According to XRD results, no new substance with fine crystallinity is observed, in consistence with samples without recrystallization (Fig. 4c). However, the characteristic peaks of recrystallized samples have obviously lower intensities than those of the unrecrystallized samples (Fig. 4c), indicating the formation of nano-sized goethite with poorer crystallinity (Fig. 4b). Except for the nano-sized goethite, another REY-bearing substance is also found under TEM observation (Fig. 5). In the recrystallized samples an amorphous floccule is noticed, and the elemental maps show that they are composed of P and REY (Fig. 5b). Meanwhile, according to ICP-MS results, a slight decline in REY concentration is shown in the recrystallized samples (GP0.2–5-Fe^{II} and GP0.2–10-Fe^{II}), with La, Ce and Lu concentrations decreased by 1–5% (Table 1). Notably, all elements are distributed evenly on the goethite surfaces.

3.5. XAFS analyses

3.5.1. La-L_1 edge XAFS

The La L_1-edge XANES (Fig. 6a) spectra of the La-adsorbed goethite before and after recrystallization are both different from that of La_2O_3 but similar to that of $La(OH)_3$ and $LaPO_4$. The feature peaks of $LaPO_4$ at ~6269 eV (A peak) and $La(OH)_3$ at ~6270 eV are very close, but their shapes are different. According to linear combination fitting (LCF), La $(OH)_3$ is not a component of any sample (Table 1). The corresponding La-adsorbed samples and $LaPO_4$ are selected to fit the recrystallized samples, and the results show that $LaPO_4$ are the major component, accounting for a minimum of ~78% (Table 1).

More details of the complexes are obtained from the EXAFS spectra. The $k^3\chi(k)$ spectra of La L_3-edge EXAFS and the corresponding RSFs (phase shift not corrected) of samples are shown in Fig. 6b and c. The uncrystallized samples exhibit the second peak at ~5 $Å^{-1}$ in the $k^3\chi(k)$ spectra, while the recrystallized ones show the peak at a higher range, 5.5–5.8 $Å^{-1}$. In R space, the La-adsorbed sample with a lower La concentration (5 mg/L, samples GP0.2–5 and GP0.2–5-Fe^{II}) exhibits a second strong peak at R + ΔR = ~3.0–3.1 Å, whereas the sample with a higher concentration (10 mg/L, sample GP0.2–10) has a weak peak at R + ΔR = 2.5–3 Å. By applying the curve-fitting method to the RSFs of the samples, the quantitative analysis illustrates that two different La···Fe distances (3.26 and 3.54 Å) are in accordance with the EXAFS spectrum of sample GP0.2–10 (Table 2). In all La-adsorbed samples, La is coordinated to nine oxygens at the distance of 2.53–2.54 Å in the first shell. The presence of a higher shell after La···Fe shell(s) is identified as La···P shell with distance of 3.87 Å.

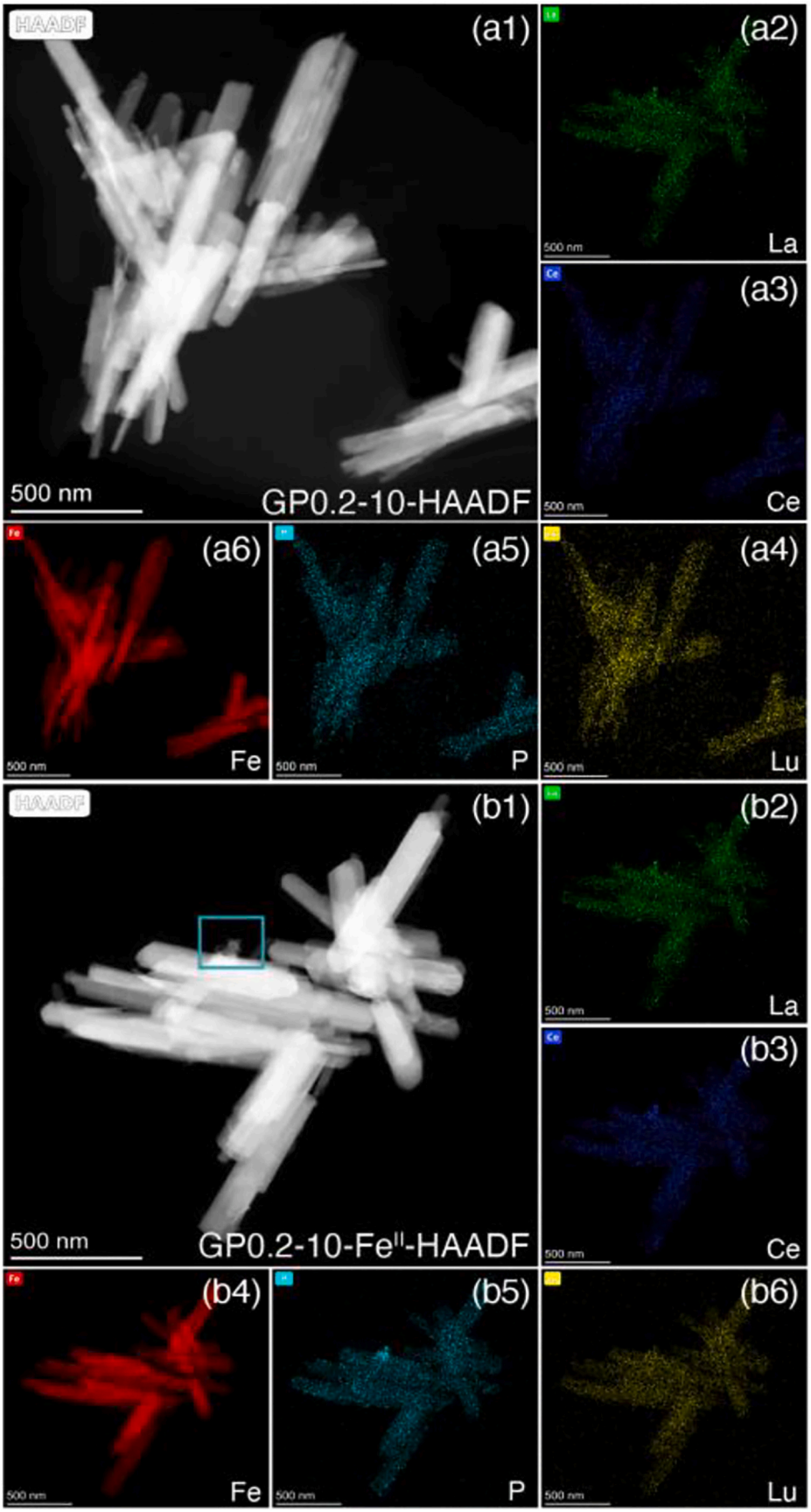

Fig. 5. TEM images and elemental maps of the REY-containing samples. TEM images of sample GP0.2–10 (pictures a1-a6) and GP0.2–10-Fe^{II} (pictures b1-b6) were acquired under HRTEM-HAADF mode. The corresponding elemental maps were for La, Ce, Lu, P and Fe (pictures a2-a6 and b2-b6). Frame in b1 emphasizes floccule of REY phosphate.

Table 1
La speciation in studied samples by linear combination fitting (LCF) of La L_1-edge EXAFS spectra. Fitting data was acquired with ATHENA.

Sample	$La(OH)_3$	La_2O_3	$LaPO_4$	GP0.2–5	GP0.2–10	Sum[a]	R factor
	%						
GP0.2–5-Fe^{II}	0	0	78(9)[a]	21(1)	/	100	0.614
GP0.2–10-Fe^{II}	0	0	100	/	0	100	0.390

[a] The uncertainties in the last digit are shown in parentheses.

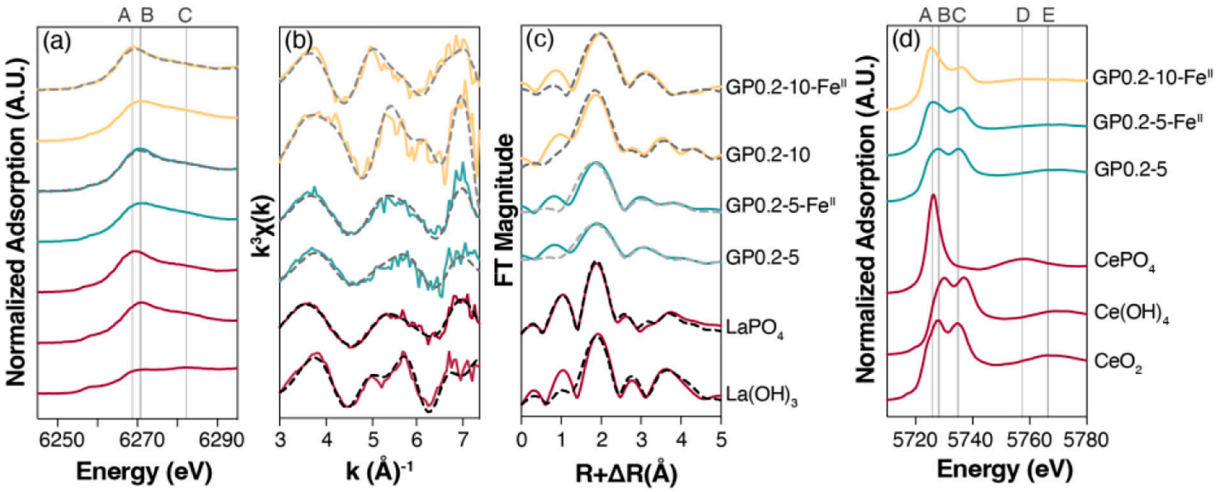

Fig. 6. La L_1-edge and Ce L_3-edge XAFS results. a, La L_1-edge XANES spectra for synthetic materials; b, k^3-weighted χ(k) spectra of La; c, RSFs (phase shift not corrected) of La; d, Ce L_3-edge XANES spectra for synthetic materials. Solid lines in pictures a-d are spectra obtained by experiments, and grey-black dash lines in pictures a, b and c are calculated spectra by a curve-fitting analysis (see data in Table S3).

3.5.2. *Ce-L_3 edge XANES*

Trivalent and tetravalent Ce species show entirely different features, as the former shows only one sharp peak and the latter one has two distinctive peaks at higher energy (Fig. 6d; Takahashi et al., 2000). Similar features are seen in the studied samples. The signature peaks of tetravalent Ce (at ~5727 eV) are dominant in the samples with lower Ce concentration (GP0.2–5), showing two strong peaks (at ~5729 eV and ~ 5735 eV) with similar intensities. Whereas in the high concentration samples (GP0.2–10 and GP0.2–10-Fe^{II}), the higher intensity of the former peak indicates that more trivalent Ce is fixed on these two samples than sample GP0.2–5.

3.6. *DFT calculations*

According to DFT calculations, the theoretical bonds of the ternary complexes are quite different on different crystal faces. Generally, there are three main adsorption faces on goethite, {001}, {021} and {110}. On {001} and {021} faces, the theoretical La—O bond is smaller (2.05–2.26 Å), but La—O bond on the {110} face is much bigger, around 2.26–2.37 Å. Besides, the La···Fe distance on {001} face is larger than La···P distance, while the La···Fe distances on the other faces overwhelm the La···P ones. The distances of 3.81 Å, 3.01–3.08 Å and 3.27–3.52 Å for La···Fe correspond to 3.37–3.38 Å, 3.37 Å and 3.88 Å for the La···P distances on {001}, {021} and {110} faces, respectively. Among them, the calculated La—O and La—Fe bond lengths in the {110} face are highly comparable to the EXAFS interpretations of La-adsorbed goethite ($R_{La\cdots Fe}$ = 3.26–3.55 Å and $R_{La\cdots P}$ = 3.87 Å, Table 2). This consistency suggests that La is predominantly adsorbed on the {110} face of goethite.

4. Discussion

4.1. *Effects of phosphate on the adsorption of synthetic goethite*

4.1.1. *Effects of phosphate*

Phosphate is an important component of porewater in shallow sediments, and in some ferromanganese (micro)nodules phosphate is positively correlated to REY and Fe contents (e.g. Hensen et al., 2005; Li et al., 2020b). Our results show that REY adsorption on goethite in groups goethite and goethite + phosphate varies with pH, but phosphate helps mitigate the negative impacts of low pH. Without P REY adsorption on goethite is substantially reduced below pH 6.0 (< 30%). Because goethite is generally positively charged under acidic conditions, REY adsorption can be limited by electrostatic repulsion between goethite and positive REY species, indicating the dominance of outer-sphere complexes. This is why laterites (< 100 ppm) formed at low pH generally have lower REY enrichment than those in hydrogenetic ferromanganese (micro)nodules (Ulrich et al., 2019), and iron oxyhydroxides including goethite may be important main hosts for middle and heavy REY (Guan et al., 2019; Li et al., 2020b). With phosphate, however, adsorption is enhanced under acidic conditions, suggesting that phosphate (0.2 mM ≥ C_P ≥ 0.02 mM) can greatly mitigate the effect of pH and hence greatly improve the adsorption capacity of goethite to ~3000 ppm. One possible explanation is that phosphate adsorbed on goethite helps neutralize the positive charge on the surface under acidic conditions, thus promoting REY adsorption. Such positive impact can be found in the co-adsorption system of Cd and phosphate by goethite (Liu et al., 2021), where Fe-P-Cd ternary complexes (phosphate-bridged) are formed.

The presence of phosphate has not only improved REY adsorption but also affects the REY enrichment patterns on goethite. In group goethite, specific adsorption of heavy REY over light REY on goethite is observed, which is consistent with the enrichment of heavy REY in deep-sea REY-rich muds (Kashiwabara et al., 2018). Interestingly, there is an

Table 2
Structural parameters of samples obtained by a curve-fitting analysis of La L_1-edge EXAFS spectra. Fitting data was obtained with ATHENA and ARTEMIS.

Sample	Shell	CN	R (Å)	ΔE_0 (eV)	σ^2 (Å^2)	χ^2_ν	R factor
$LaPO_4$	La-O	9.1 (6)[a]	2.39 (9)	6(8)	0.003 (1)	128	0.023
	La-P	3	3.13 (5)		0.018 (4)		
	La-La	2	3.98 (1)		0.007		
$La(OH)_3$	La-O	8.6 (9)	2.39 (9)	-3(7)	0.011 (6)	156	0.019
	La-La_1	2	3.74 (2)		0.001 (1)		
	La-La_2	6	4.27 (9)		0.002 (8)		
GP0.2–5	La-O	8.9 (8)	2.53 (6)	-4(8)	0.015 (5)	32	0.026
	La···Fe2	1	3.55 (6)		0.012 (5)		
	La···P	1	3.87 (2)		0.004 (6)		
GP0.2–5-Fe^{II}	La-O	9.3 (1)	2.56 (3)	-4(9)	0.003 (1)	50	0.025
	La···P	3	3.14 (1)		0.010 (7)		
	La···Fe2	1	3.49 (6)		0.003 (1)		
GP0.2–10	La-O	9.0 (2)	2.54 (2)	-2(1)	0.005 (8)	58	0.023
	La···Fe1	0.5	3.26 (4)		0.016 (2)		
	La···Fe2	1	3.54 (9)		0.011 (3)		
	La···P	1	3.87 (6)		0.002 (5)		
GP0.2–10-Fe^{II}	La-O	8.9 (6)	2.71 (4)	2(3)	0.013 (8)	69	0.023
	La-P	3	3.18 (9)		0.003 (5)		

CN: coordination number; R: interatomic distance; ΔE_0: threshold E_0 shift; σ^2: Debye-Waller factor; χ^2_ν: reduced chi-square value.
[a] The uncertainties in the last digit for CN, R, ΔE_0, and σ^2 are reported in parentheses.

obvious tetrad effect that grows stronger as C_{REY} increases (Fig. 3c and f). However, the REY adsorption on goethite does not always increase with the elevated REY concentrations; it declines at higher concentrations ($\geq$ 0.5 mg/L) probably due to the high IS caused by increasing REY concentration. In the co-adsorption system of phosphate, the negatively charged oxyanions increase the REY, especially light REY adsorption on goethite geometrically and even exponentially at high REY concentration (1 mg/L; Fig. 3f and Fig. S3).

4.1.2. Effects of high IS and carbonate

To make the simulation conditions closer to the seawater environment, samples treated with high IS and REY-carbonate complexes are also studied. Although the REY adsorption in groups goethite and goethite + phosphate is both notably influenced by high IS (0.5 M $NaNO_3$; similar to that of seawater), adsorption of REY during co-adsorption is still substantially increased compared to group goethite and the adsorption patterns of REY remain unchanged (Table S7). And importantly, the role that carbonate plays during REY adsorption seems to be the same as phosphate, both of which significantly accelerate the REY adsorption on goethite and also reinforce the adsorption capacity of goethite (up to 2000 ppm for La in sample GP0.2–10). However, according to the FT-IR analytical results exerted by Ohta and Kawabe (2000), no feature peaks of carbonate are shown in the spectra of Fe^{III} precipitates with REY^{III} adsorbed. These observations indicate that goethite can rapidly scavenge REY from seawater while leaving carbonate in solution; and because of the extremely low REY content in seawater, the REY pattern should be identical to seawater.

4.1.3. Adsorption mechanisms

For better understanding of how P, goethite and REY are positively related in some (micro)nodules, the adsorption mechanisms of REY on phosphate-adsorbed goethite are investigated. Physical interactions (forming outer-sphere complexes), chemical binding (forming inner-sphere complexes), surface precipitation and/or lattice substitution always occur during cations immobilization.

The simulation results of the saturation pH of rare earth hydroxide under the same conditions suggests no precipitation is formed under pH 6.8 (Gustafsson, 2018). The adsorption kinetics data of REY on goethite were simulated with the pseudo-first-order and pseudo-second-order models (equations referred to Qin et al., 2021). Fig. 3a shows a better agreement between kinetic data and the pseudo-second-order model ($R^2 = 0.98$), which implies the adsorption of REY on goethite in goethite is dominated by chemical binding rather than physical interactions (Wu et al., 2018). More importantly, if substitution occurs during the adsorption, the crystal structure and characteristic peaks of goethite could change. However, according to XRD and SEM analyses goethite grains are observed with no structural changes in either micro or nanoscale, meaning neither lattice substitution nor new substances formed in both reaction systems during the aerobic adsorption of REY. Therefore, goethite mainly immobilizes REY via chemical interaction and the possibility of surface precipitation and lattice substitution is excluded.

Subsequent desorption results give more detailed information about the adsorption mechanism. Generally, two kinds of complexations are formed during adsorption, outer-sphere, and inner-sphere complexations. As outer-sphere complexes are formed via physical interactions, they are easily extracted by weak complexing agent such as CH_3COONH_4 (Wu et al., 2018). On the other hand, the chemically bonded inner-sphere complexes can be easily leached by a stronger desorption agent like EDTA-2Na. Our result shows up to ~87% of adsorbed REY remained in the residue. According to the desorption results, there should be few or no REY precipitations are formed during REY adsorption by goethite at pH 6.8. Therefore, the residual phase can be stronger inner-sphere complexes (Borst et al., 2020). The dominating fractions of inner-sphere complexes shown in the desorption experiments also agree well with the kinetic data, indicating that REY and phosphate mainly combine with goethite via inner-sphere complexation. As a result, we conclude that the REY (except for Ce) are adsorbed on goethite mainly through inner-sphere complexation.

The adsorption configurations of REY on goethite were obtained from the XAFS spectra of the uncrystallized samples. The LCF results of La L_1-edge XAFS spectra of the La-adsorbed goethite before recrystallization show that $La(OH)_3$ is not the component of the samples, further denying the possible existence of REY hydroxides precipitation. The presence of the higher La—Fe and La—P shells after La—O shell and the corresponding distances indicate the formation of ternary complexes. The higher-shell contributions in uncrystallized samples are best fit at ~3.55 Å for La···Fe and ~ 3.87 Å for La···P, which are in better coordination with the configuration we optimized for La^{III} and phosphate on goethite clusters in face {110} by DFT calculations, rather than the {001} or {021} faces. Both the EXAFS interpretations and DFT calculations suggest that on the {110} face, La and phosphate share one oxygen atom and bind separately to two adjacent oxygen atoms on the goethite surface to form ternary complexes. A similar preference for adsorption positions is also discovered in the Sc adsorption on goethite (Qin et al., 2021). Additionally, two different La···Fe distances (3.26 and 3.54 Å) identified in EXAFS imply another kind of complexes may formed in high La solution during adsorption, and the complexes can be binary complexes of REY and goethite due to excessive REY.

As a redox sensitive element, Ce does not behave the same as La during adsorption, but with the help of dissolved oxygen some Ce is

fixed on goethite in a different way. In this case, some Ce^{III} ions are oxidized on the goethite surface during adsorption. During the experiment, the content of each REY in REY reaction solution is monitored and there is no significant decrease in Ce content after the solution is filtrated and analyzed with ICP-MS. Considered that 1) if Ce^{III} is directly oxidized by dissolved oxygen, Ce^{IV} oxides will form and precipitate, and 2) the redox potential of Ce^{IV}-Ce^{III} (1.42–1.50 V) is much higher than that of Fe^{II}-goethite (~ 0.24 V) at room temperature (Paulenova et al., 2002; Hu et al., 2021), Ce^{III} should be oxidized by dissolved oxygen under the catalysis of goethite. Due to the limited amount of dissolved oxygen, however, the valence of the extra Ce^{III} in high Ce solutions remains unchanged, whose feature peak overwrites the first peak of Ce^{IV} (Fig. 6d), similar to the XANES results for REY-rich muds in Pacific Ocean (Kashiwabara et al., 2018).

In conclusion, goethite mainly adsorbs REY through inner-sphere complexation without phosphate. In samples with phosphate, ternary complexes are formed with phosphate linking REY and Fe on goethite, and most REY are fixed on the face {110}. More importantly, due to limited oxygen, some redox sensitive Ce is oxidized shortly after adsorption by goethite.

4.2. REY release during recrystallization

Goethite recrystallization is common in early diagenesis of (micro) nodules. In our study, the ICP-MS and XAFS analyses indicate that both light and heavy REY are released during goethite recrystallization (Table S10 and 2), and meanwhile, IOH is formed according to the XRD and STEM results. Apart from that, a flocculent mineral attached to goethite is also noticed in the recrystallized samples when compared to that of uncrystallized ones and is identified as REY phosphate via elemental mapping results (Fig. 5b). Precipitation of REY phosphate indicates the release of REY and phosphate, implying the fixation of REY on goethite is weakened after recrystallization and aging for 21 days (Mustafa et al., 2006), causing the precipitation of phosphate and REY^{III}.

In the meanwhile, some of the previous adsorbed and oxidized Ce^{IV} on goethite is partly reduced to Ce^{III} during recrystallization, showing a significantly higher peak at ~5727 eV than another peak (Fig. 6d). Considered that the redox potential of Ce^{IV}-Ce^{III} (1.42–1.50 V) is much higher than that of Fe^{II}-goethite (~ 0.24 V) at room temperature (Paulenova et al., 2002; Hu et al., 2021), Ce^{IV} can be easily reduced and release during recrystallization. It is suggested that after the recrystallization and dissolution of goethite, the previously fixed Ce^{IV} is reduced and released, and can be subsequently fixed by other REY hosts, and the intensity of Ce-reduction reaction generally increases with depth (Takahashi et al., 2015). In this scenario, the Ce anomalies possessed by goethite or other dissolved ferromanganese (oxy)hydroxides/oxides can be passed down after their dissolution. This observation provides explanation for the positive Ce anomalies shown in bioapatite and coincides with the previous suggestion that the positive Ce anomaly of apatite must can be inherited from its previous hosts of ferromanganese (micro)nodules (Takahashi et al., 2015; Liao et al., 2019, 2022; Zhou et al., 2020).

During the reductive dissolution of goethite, some cations may enter its lattice (Frierdich and Catalano, 2012). However, attempts to synthesize La/Lu-substituted goethite revealed the coexistence of acicular goethite and an unidentified discoid La/Lu-mineral when their proportions exceeded 0.1% in the bath solution (Fig. S6). This observation indicates that either La or Lu incorporation into goethite is challenging due to their larger ionic radius differences with Fe (Cornell and Schwertmann, 2003). Furthermore, the $LaPO_4$ identified in XAFS analyses of recrystallized samples suggests that most La are desorbed (Fig. 6 and Table 1). However, since goethite inevitably possesses lattice defects in both natural and laboratory-synthesized samples (Hou et al., 2022), the possibility of lattice substitution cannot be excluded, especially in the newly formed IOH.

In conclusion, REY adsorbed on goethite are massively released, and the tetravalent Ce is partially reduced and then released after recrystallization for 21 days, which indicates that these reactivated Ce^{III} can be transported along porewater to find their next hosts. The observations are consistent with the positive Ce anomaly showed in the REY distribution patterns of ferromanganese oxides and bioapatite suggesting that not only manganese oxides, generally considered to be MnO_2, but also iron (oxy)hydroxides can help passing positive Ce anomaly to bioapatite. Although manganese oxides are considered to be main providers of positive Ce anomaly in sediments (Koeppenkastrop and De Carlo, 1992; Takahashi et al., 2000), the role of iron minerals should not be neglected (Liao et al., 2022).

4.3. Implications for REY enrichment during early diagenesis

Combining the synthetic goethite adsorption experiments with previously published research on marine (micro)nodules and bioapatite, we have a clearer view of REY enrichment and variations of REY/REY-carbonate distribution patterns between two hosts during early diagenesis. Our study elucidates the followings: 1) According to batch adsorption, the presence of phosphate and carbonate elevates the adsorption of light REY (as goethite preferentially adsorbed heavy REY in solution without phosphate and carbonate) and substantially increases the REY adsorption capacity of goethite. 2) At molecular-scale, REY are immobilized by forming inner-sphere or ternary complexes with phosphate on the predominant {110} face of goethite. 3) Different from other REY, Ce^{III} can be subsequently oxidized by dissolved oxygen on the goethite surface under oxic conditions. 4) Furthermore, most of the adsorbed REY are released during recrystallization under hypoxic conditions, which possibly controls the redistribution of REY in deep-sea sediments.

These findings allow a clearer schematic model of how REY (except for Ce) and Ce are scavenged by goethite near the oxic-suboxic frontier (OSF) is established (Fig. 7). In the oxic zone (Fig. 7a), REY enrichment is relatively low in goethite and other ferromanganese oxides (Fig. 7b) due to the extremely low REY concentration of seawater and shallow porewater (Hensen et al., 2005). However, with carbonate complexed REY can be scavenged efficiently. In the zone where the impact of seawater overwhelms porewater, iron oxyhydroxides scavenge REY through inner-sphere (major) and outer-sphere complexation (minor), with the REY patterns identical to seawater. Meanwhile, with sufficient oxygen (Fig. 7a), Ce can be oxidized and fixed on the iron oxyhydroxides (Fig. 7b) and manganese oxides (Takahashi et al., 2000; Kashiwabara et al., 2018). Because both oxides are the main REY hosts during this period, if they scavenge all REY in similar adsorption rates form seawater and fix Ce by oxidation, their REY pattern should be the same as seawater except for a strong positive Ce anomaly (Fig. 7c).

In the sub-oxic zone where (micro)nodules are buried deeper, with continuous consumption of oxygen and rising phosphate concentration (Hensen et al., 2005; Mizell and Hein, 2015; Ren et al., 2022), manganese oxides start to reduce and release massive REY ions at OSF (Fig. 7a). With the help of phosphate, REY released by manganese oxides can be rapidly adsorbed to the adjacent iron oxyhydroxides, forming ternary complexes of REY and phosphate (Fig. 7b). Meanwhile, some REY can also be transferred to (bio)apatite through porewater, and at this point, competition for REY inevitably happens between iron oxyhydroxides and bioapatite. The REY pattern of iron oxyhydroxide is still similar to seawater, but with a weakened positive Ce anomaly due to the reduction and release of some Ce^{IV} as Mn minerals dissolve (Fig. 7c).

In the hypoxic zone (Fig. 7a), as burial depth increases, reduction dissolution of iron oxyhydroxides starts. Less stable iron oxyhydroxides are reduced first, releasing REY and Fe^{II}. The released REY are ultimately transferred to different hosts (most likely bioapatite) or diffuse towards the oxic zone for another cycle during the early diagenesis. Under such circumstances, Ce^{IV} will be reduced and released, and the reduction grows stronger with depth. In the meanwhile, massive release of Ce enables the adjacent porewater or their new hosts (e.g., apatite) to

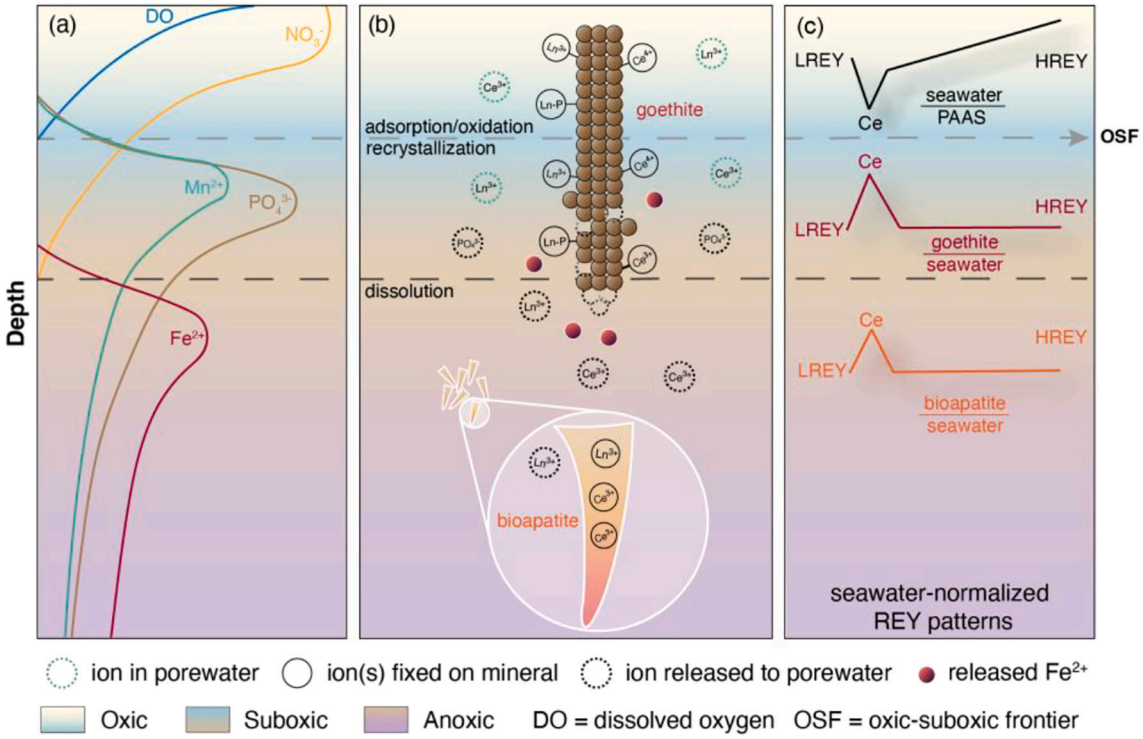

Fig. 7. Schematic scavenging-transfer model of REY near the OSF. a, Distribution of oxidants and reductants in marine sediment; b, the geochemical behavior of REY in marine sediment; c, simplified Post-Archean Australian Shale-normalized (PAAS; Taylor and McLennan, 1985) REY pattern of seawater and seawater-normalized REY patterns of goethite and bioapatite. In the oxic zone, REY are termed Ln here, and goethite initially adsorbs Ln and oxidizes Ce (circles with black solid lines) from seawater/porewater (circles with green dashed lines) in the sediment; In the suboxic zone, manganese oxides dissolve and release REY (circles with black dashed lines), which is subsequently adsorbed on the adjacent iron oxyhydroxides with the help of phosphate or incorporated into the bioapatite nearby; In the hypoxic zone, iron oxyhydroxides recrystallize and release the rest of the adsorbed REY to the porewater (circles with black dashed lines) or bioapatite, and the Ce anomalies possessed by ferromanganese oxides are passed onto bioapatite. Light and heavy REY are termed as LREY and HREY, respectively. All REY ions in seawater/porewater are complexed with carbonate. (For interpretation of the references to colour in this figure legend, the reader is referred to the web version of this article.)

inherit the positive Ce anomalies previously possessed by ferromanganese minerals (Fig. 7c). Our observations provide evidence for iron oxyhydroxides being efficient but transient repositories of REY, which indicates that the positive Ce anomaly of apatite can be inherited from ferromanganese oxides during early diagenesis.

5. Conclusions

Our study simulates how REY are adsorbed by iron oxyhydroxides from seawater and then released to porewater under hypoxic conditions, likely leading to their transferal to bioapatite (fish teeth and bones). Our observations are in good agreement with REY abundance and distribution in natural samples. In summary, we find that firstly, goethite can adsorb REY (especially heavy REY) and the adsorption efficiency increases geometrically in the presence of phosphate, while during aerobic adsorption, the adsorbed Ce^{III} is further oxidized to Ce^{IV} on the goethite surface by dissolved oxygen. Secondly, almost all REY are released during goethite recrystallization in hypoxic environment; notably, Ce^{IV} is also reduced and released during recrystallization. Finally, our experiments demonstrate that iron oxyhydroxides and phosphate play a crucial role in REY enrichment during early diagenesis.

CRediT authorship contribution statement

Yongjia Liang: Writing – original draft. **Xiaoming Sun:** Writing – review & editing, Supervision, Project administration, Conceptualization. **Dengfeng Li:** Writing – review & editing, Investigation. **Caroline L. Peacock:** Writing – review & editing. **Yu Fu:** Investigation.

Declaration of competing interest

The authors declare no competing financial interests.

Data availability

Data will be made available on request.

Acknowledgments

This work was financially supported by the National Natural Science Foundation of China (Nos.92262304, 42272066 and U2244222) and the National Key Research and Development Program of China (No.2018YFA0702605). We also thank Drs. Yundang Wu, Yanping Zhu, and Jing Liu for their inspiring comments and discussions, and many thanks to Dr. Sanyuan Zhu for his great support in XAFS analysis and use of Athena.

Appendix A. Supplementary data

Supplementary materials contain a series of ten supplementary tables and six figures. Table S1 and S2 are the previously published data used in Fig. 1 and Fig. 2, respectively. Table S3-S9 are the REY adsorption and desorption data of REY/REY-carbonate on goethite. For supplementary figures, Figs. S1 and S2 are the XRD patterns and morphology of goethite, respectively; Figs. S3 and S4 are the ICP-MS results of REY adsorption with high IS and REY-carbonate adsorption on goethite, respectively; Fig. S5 is the XRD patterns of REY-adsorbed goethite; Fig. S6 is the SEM images of La- and Lu-substituted goethite.

References

Antelo, J., Avena, M., Fiol, S., López, R., Arce, F., 2005. Effects of pH and ionic strength on the adsorption of phosphate and arsenate at the goethite-water interface. J. Colloid Interface Sci. 285, 476–486. https://doi.org/10.1016/j.jcis.2004.12.032.

Bau, M., 1999. Scavenging of dissolved yttrium and rare earths by precipitating iron oxyhydroxide: Experimental evidence for Ce oxidation, Y-Ho fractionation, and lanthanide tetrad effect. Geochim. Cosmochim. Acta 63 (1), 67–77. https://doi.org/10.1016/j.jcis.2004.12.032.

Borst, A.M., Smith, M.P., Finch, A.A., Estrade, G., Villanova-de-Benavent, C., Nason, P., Marquis, E., Horsburgh, N.J., Goodenough, K.M., Xu, C., Kynický, J., Geraki, K., 2020. Adsorption of rare earth elements in regolith-hosted clay deposits. Nat. Commun. 11, 1–15. https://doi.org/10.1038/s41467-020-17801-5.

Cornell, R.M., Schwertmann, U., 2003. The Iron Oxides: Structure, Properties, Reactions, Occurences and Uses, second ed. Wiley-VCH, Germany. https://doi.org/10.1002/3527602097. pp 1-7, 42-51.

Dekov, V.M., Marchig, V., Rajta, I., Uzonyi, I., 2003. Fe-Mn micronodules born in the metalliferous sediments of two spreading centres: the East Pacific rise and Mid-Atlantic Ridge. Mar. Geol. 199, 101–121. https://doi.org/10.1016/S0025-3227(03)00124-5.

Frierdich, A.J., Catalano, J.G., 2012. Controls on Fe(II)-activated trace element release from goethite and hematite. Environ. Sci. Technol. 46, 1519–1526. https://doi.org/10.1021/es203272z.

Giannozzi, P., Baroni, S., Bonini, N., Calandra, M., Car, R., Cavazzoni, C., Ceresoli, D., Chiarotti, G.L., Cococcioni, M., Dabo, I., Dal Corso, A., de Gironcoli, S., Fabris, S., Fratesi, G., Gebauer, R., Gerstmann, U., Gougoussis, C., Kokalj, A., Lazzeri, M., Martin-Samos, L., Marzari, N., Mauri, F., Mazzarello, R., Paolini, S., Pasquarello, A., Paulatto, L., Sbraccia, C., Scandolo, S., Sclauzero, G., Seitsonen, A.P., Smogunov, A., Umari, P., Wentzcovitch, R.M., 2009. QUANTUM ESPRESSO: a modular and open-source software project for quantum simulations of materials. J. Phys. Condens. Matter 21, 395502. https://doi.org/10.1088/0953-8984/21/39/395502.

Gorski, C.A., Fantle, M.S., 2017. Stable mineral recrystallisation in low temperature aqueous systems: a critical review. Geochim. Cosmochim. Acta 198, 439–465. https://doi.org/10.1016/j.gca.2016.11.013.

Guan, Y., Ren, Y., Sun, X., Xiao, Z., Wu, Z., 2019. Fine scale study of major and trace elements in the Fe-Mn nodules from the South China Sea and their metallogenic constraints. Mar. Geol. 416, 105978. https://doi.org/10.1016/j.margeo.2019.105978.

Gustafsson, J.P., 2018. Visual MINTEQ, Version 3.1; Department of Land and Water Resources Engineering. KTH: (Royal Institute of Technology), Stockholm. Available for free download at the website of. http://vminteq.lwr.kth.se/download/.

Hensen, C., Zabel, M., Schulz, H.N., 2005. Marine Geochemistry. In: Springer, H.D., Schulz, M. Zabel (Eds.), Benthic Cycling of Oxygen, Nitrogen and Phosphorus. Berlin, pp. 207–234. https://doi.org/10.1007/3-540-32144-6.

Hinkle, M.A.G., Catalano, J.G., 2015. Effect of phosphate and sulfate on Ni repartitioning during Fe(II)-catalyzed Fe(III) oxide mineral recrystallization. Geochim. Cosmochim. Acta 165, 62–74. https://doi.org/10.1016/j.gca.2015.05.032.

Hou, J., Tan, X., Xiang, Y., Zheng, Q., Chen, C., Sha, Z., Ren, L., Wang, M., Tan, W., 2022. Insights into the underlying effect of Fe vacancy defects on the adsorption affinity of goethite for arsenic immobilization. Environ. Pollut. 314, 120268. https://doi.org/10.1016/j.envpol.2022.120268.

Hu, S., Liu, T., Yang, Y., Li, F., Fang, L., 2021. Cysteine induced cascade electron transfer by forming a unique ternary complex with Fe(II) on goethite. Chem. Geol. 584, 120561 https://doi.org/10.1016/j.chemgeo.2021.120561.

Jaisi, D.P., Dong, H., Plymale, A.E., Fredickson, J.K., Zachara, J.M., Heald, S., Liu, C., 2009. Reduction and long-term immobilization of technetium by Fe(II) associated with clay mineral nontronite. Chem. Geol. 264 (1–4), 127–138. https://doi.org/10.1016/j.chemgeo. 2009.02.018.

Kashiwabara, T., Toda, R., Nakamura, K., Yasukawa, K., Fujinaga, K., Kubo, S., Nozaki, T., Takahashi, Y., Suzuki, K., Kato, Y., 2018. Synchrotron X-ray spectroscopic perspective on the formation mechanism of REY-rich muds in the Pacific Ocean. Geochim. Cosmochim. Acta 240, 274–292. https://doi.org/10.1016/j.gca.2018.08.013.

Kato, Y., Fujinaga, K., Nakamura, K., Takaya, Y., Kitamura, K., Ohta, J., Toda, R., Nakashima, T., Iwamori, H., 2011. Deep-sea mud in the Pacific Ocean as a potential resource for rare-earth elements. Nat. Geosci. 4, 535–539. https://doi.org/10.1038/ngeo1185.

Koeppenkastrop, D., De Carlo, E.H., 1992. Sorption of rare-earth elements from seawater onto synthetic mineral particles: an experimental approach. Chem. Geol. 95 (3–4), 251–263. https://doi.org/10.1016/0009-2541(92)90015-W.

Li, D., Fu, Y., Liu, Q., Reinfelder, J.R., Hollings, P., Sun, X., Tan, C., Dong, Y., Ma, W., 2020a. High-resolution LA-ICP-MS mapping of deep-sea polymetallic micronodules and its implications on element mobility. Gondwana Res. 81, 461–474. https://doi.org/10.1016/j.gr.2019.12.009.

Li, D., Fu, Y., Sun, X., Wei, Z., 2020b. Critical metal enrichment mechanism of deep-sea hydrogenetic nodules: Insights from mineralogy and element mobility. Ore Geol. Rev. 118, 103371 https://doi.org/10.1016/j.gr.2019.12.009.

Liao, J., Sun, X., Wu, Z., Sa, R., Guan, Y., Lu, Y., 2019. Fe-Mn (oxyhydr)oxides as an indicator of REY enrichment in deep-sea sediments from the central North Pacific. Ore Geol. Rev. 112, 103044 https://doi.org/10.1016/j.oregeorev.2019.103044.

Liao, J., Chen, J., Sun, X., Wu, Z., Deng, Y., Shi, X., Wang, Y., Chen, Y., Koschinsky, A., 2022. Quantifying the controlling mineral phases of rare-earth elements in deep-sea pelagic sediments. Chem. Geol. 595, 120792 https://doi.org/10.1016/j.chemgeo.2022.120792.

Liu, J., Zhu, R., Ma, L., Fu, H., Lin, X., Parker, S.C., Molinari, M., 2021. Adsorption of phosphate and cadmium on iron (oxyhydr)oxides: a comparative study on ferrihydrite, goethite, and hematite. Geoderma 383, 114799. https://doi.org/10.1016/j.geoderma.2020.114799.

Masuda, A., Ikeuchi, Y., 1979. Lanthanide tetrad effect observed in marine environment. Geochem. J. 13, 19–22. https://doi.org/10.2343/geochemj.13.19.

Menendez, A., James, R., Roberts, S., Peel, K., Connelly, D., 2017. Controls on the distribution of rare earth elements in deep-sea sedi- ments in the North Atlantic Ocean. Ore Geol. Rev. 2017 (87), 100–113. https://doi.org/10.1016/j.oregeorev.2016.09.036.

Mimura, K., Nakamura, K., Yasukawa, K., Machida, S., Ohta, J., Fujinaga, K., Kato, Y., 2019. Significant impacts of pelagic clay on average chemical composition of subducting sediments: New insights from discovery of extremely rare-earth elements and yttrium-rich mud at Ocean Drilling Program Site 1149 in the western North Pacific Ocean. J. Asian Earth Sci. 186, 104059 https://doi.org/10.1016/j.jseaes.2019.104059.

Mizell, K., Hein, J.R., 2015. Encyclopedia of Earth Sciences Series. In: White, W.M. (Ed.), Ferromanganese Crusts and Nodules: Rocks that Grow. Springer, pp. 477–482. https://doi.org/10.1007/978-3-319-39312-4_101.

Mustafa, G., Kookana, R.S., Singh, B., 2006. Desorption of cadmium from goethite: Effects of pH, temperature and aging. Chemosphere 64, 856–865. https://doi.org/10.1016/j.chemosphere.2005.10.041.

Ohta, A., Kawabe, I., 2000. Rare earth element partitioning between Fe oxyhydroxide precipitates and aqueous NaCl solutions doped with $NaHCO_3$: Determinations of rare earth element complexation constants with carbonate ions. Geochim. Cosmochim. Acta 34 (6), 439–454. https://doi.org/10.2343/geochemj.34.439.

Ohta, A., Kawabe, I., 2001. REE(III) adsorption onto Mn dioxide (δ-MnO_2) and Fe oxyhydroxide: Ce(III) oxidation by δ-MnO_2. Geochim. Cosmochim. Acta 65 (5), 695–703. https://doi.org/10.1016/S0016-7037(00)00578-0.

Pattan, J.N., Rao, C.M., Higgs, N.C., Colley, S., Parthiban, G., 1995. Distribution of major, trace and rare-earth elements in surface sediments of the Wharton Basin, Indian Ocean. Chem. Geol. 121, 201–215. https://doi.org/10.1016/0009-2541(94)00112-L.

Paulenova, A., Creager, S.E., Navratil, J.D., Wei, Y., 2002. Redox potentials and kinetics of the Ce^{3+}/Ce^{4+} redox reaction and solubility of cerium sulfates in sulfuric acid solutions. J. Power Sources 109, 431–438. https://doi.org/10.1016/S0378-7753(02)00109-X.

Peacock, C.L., Sherman, D.M., 2004. Vanadium(V) adsorption onto goethite (α-FeOOH) at pH 1.5 to 12: a surface complexation model based on ab initio molecular geometries and EXAFS spectroscopy. Geochim. Cosmochim. Acta 68, 1723–1733. https://doi.org/10.1016/j.gca.2003.10.018.

Persson, P., Nilsson, N., Sjöberg, S., 1996. Structure and bonding of orthophosphate ions at the iron Oxide–Aqueous interface. J. Colloid Interface Sci. 177, 263–275. https://doi.org/10.1006/jcis.1996.0030.

Qin, H.B., Yang, S., Tanaka, M., Sanematsu, K., Arcilla, C., Takahashi, Y., 2021. Scandium immobilization by goethite: Surface adsorption versus structural incorporation. Geochim. Cosmochim. Acta 294, 255–272. https://doi.org/10.1016/j.gca.2020.11.020.

Ren, J., Jiang, X., He, G., Wang, F., Yang, T., Luo, S., Deng, Y., Zhou, J., Deng, X., Yao, H., Yu, H., 2022. Enrichment and sources of REY in phosphate fractions: Constraints from the leaching of REY-rich deep-sea sediments. Geochim. Cosmochim. Acta 335, 155–168. https://doi.org/10.1016/j.gca.2022.08.035.

Sancho-García, J.C., Brédas, J.L., Cornil, J., 2003. Assessment of the reliability of the Perdew-Burke-Ernzerhof functionals in the determination of torsional potentials in π-conjugated molecules. Chem. Phys. Lett. 377, 63–68. https://doi.org/10.1016/S0009-2614(03)01086-8.

Sattarova, V., Astakhov, A., Aksentov, K., Shi, X., Hu, L., Liu, Y., Polyakov, D., Alatortsev, A., Kolesnik, O., 2023. Geochemistry of the Laptev and East Siberian seas sediments with emphasis on rare-earth elements: Application for sediment sources and paleoceanography. Cont. Shelf Res. 254, 104907 https://doi.org/10.1016/j.csr.2022.104907.

Shannon, R.D., 1976. Revised effective ionic radii and systematic studies of interatomic distances in halides and chalcogenides. Acta Crystallogr. A32, 751–767. https://doi.org/10.1107/S0567739476001551.

Takahashi, Y., Shimizu, H., Usui, A., Kagi, H., Nomura, M., Akahashi, Y.O.T., Himizu, H. I.S., Sui, A.K.U., Agi, H.I.K., Omura, M.A.N., 2000. Direct observation of tetravalent cerium in ferromanganese nodules and crusts by X-ray-absorption near-edge structure (XANES). Geochim. Cosmochim. Acta 64, 2929–2935. https://doi.org/10.1016/S0016-7037(00)00403-8.

Takahashi, Y., Manceau, A., Geoffroy, N., Marcus, M.A., Usui, A., 2007. Chemical and structural control of the partitioning of Co, Ce, and Pb in marine ferromanganese oxides. Geochim. Cosmochim. Acta 71, 984–1008. https://doi.org/10.1016/j.gca.2006.11.016.

Takahashi, Y., Hayasaka, Y., Morita, K., Kashiwabara, T., Nakada, R., Marcus, M.A., Kato, K., Tanaka, K., Shimizu, H., 2015. Transfer of rare earth elements (REE) from manganese oxides to phosphates during early diagenesis in pelagic sediments inferred from REE patterns, X-ray absorption spectroscopy, and chemical leaching method. Geochem. J. 49, 653–674. https://doi.org/10.2343/geochemj.2.0393.

Tanaka, E., Nakamura, K., Yasukawa, K., Mimura, K., Fujinaga, K., Iijima, K., Nozaki, T., Kato, Y., 2020. Chemostratigraphy of deep- sea sediments in the western North Pacific Ocean: Implications for genesis of mud highly enriched in rare-earth elements and yttrium. Ore Geol. Rev. 119, 103392. https://doi.org/10.1016/j.oregeorev.2020.103392.

Tang, J., Johannesson, K.H., 2010. Ligand extraction of rare earth elements from aquifer sediments: Implications for rare earth element complexation with organic matter in natural waters. Geochim. Cosmochim. Acta 74, 6690–6705. https://doi.org/10.1016/j.gca.2010.08.028.

Taylor, S.D., Marcano, M.C., Becker, U., 2017. A first principles investigation of electron transfer between Fe(II) and U(VI) on insulating Al- vs. semiconducting Fe-oxide surfaces via the proximity effect. Geochim. Cosmochim. Acta 197, 305–322. https://doi.org/10.1016/j.gca.2016.10.022.

Taylor, S.R., McLennan, S.M., 1985. The continental crust: its composition and evolution. In: An Examination of the Geo-Chemical Record Preserved in Sedimentary Rocks. https://doi.org/10.1086/629067.

Ulrich, M., Cathelineau, M., Muñoz, M., Boiron, M.C., Teitler, Y., Karpoff, A.M., 2019. The relative distribution of critical (Sc, REE) and transition metals (Ni, Co, Cr, Mn, V) in some Ni-laterite deposits of New Caledonia. J. Geochem. Explor. 197, 93–113. https://doi.org/10.1016/j.gexplo.2018.11.017.

Vereshchagin, O.S., Perova, E.N., Brusnitsyn, A.I., Ershova, V.B., Khudoley, A.K., Shilovskikh, V.V., Molchanova, E., 2019. Ferro-manganese nodules from the Kara Sea: Mineralogy, geochemistry and genesis. Ore Geol. Rev. 106, 192–204. https://doi.org/10.1016/j.oregeorev.2019.01.023.

Weng, Z., Jowitt, S.M., Mudd, G.M., Haque, N., 2015. A detailed assessment of global rare earth element resources: opportunities and challenges. Econ. Geol. 110, 1925–1952. https://doi.org/10.2113/econgeo.110.8.1925.

Wu, C., Lei, Chen, Yang, S., Cai, Y., Xu, L., Wu, X., Qin, H., Liu, Z., Lanhua, Chen, Wang, S., 2018. Macroscopic, theoretical simulation and spectroscopic investigation on the immobilization mechanisms of Ni(II) at cryptomelane/water interfaces. Chemosphere 210, 392–400. https://doi.org/10.1016/j.chemosphere.2018.07.029.

Yasukawa, K., Nakamura, K., Fujinaga, K., Iwamori, H., Kato, Y., 2016. Tracking the spatiotemporal variations of statistically independent components involving enrichment of rare-earth elements in deep-sea sediments. Sci. Rep. 6, 29603. https://doi.org/10.1038/srep29603.

Yasukawa, K., Ohta, J., Mimura, K., Tanaka, E., Takaya, Y., Usui, Y., Fujinaga, K., Machida, S., Nozaki, T., Iijima, K., Nakamura, K., Kato, Y., 2018. A new and prospective resource for scandium: evidence from the geochemistry of deep-sea sediment in the western North Pacific Ocean. Ore Geol. Rev. 102, 260–267. https://doi.org/10.1016/j.oregeorev.2018.09.001.

Zhang, X., Huang, M., Shi, X., Huang, D., 2019. The geochemical characteristics of rare earth elements rich deep sea deposit of Core GC11 in Central Indian Ocean Basin. Haiyang Xuebao 41, 51–61. https://doi.org/10.3969/j.issn.0253-4193.2019.12.005.

Zhou, T., Shi, X., Huang, M., Yu, M., Bi, D., Ren, X., Yang, G., Zhu, A., 2020. The influence of hydrothermal fluids on the REY-rich deep-sea sediments in the Yupanqui basin, eastern South Pacific Ocean: constraints from bulk sediment geochemistry and mineralogical characteristics. Minerals 10, 1–23. https://doi.org/10.3390/min10121141.